CSIRO PUBLISHING

Exploration Geophysics, 2018, **49**, 891–897
https://doi.org/10.1071/EG17018

Acoustic VTI reverse time migration based on an improved source wavefield storage strategy

Ying Shi[1,3] Xiuzheng Fang[2] Weihong Wang[1] Xuan Ke[1]

[1]Northeast Petroleum University, School of Earth Science, Daqing, Heilongjiang 163318, China.
[2]The Unconventional Natural Gas Institute, China University of Petroleum, Beijing 102249, China.
[3]Corresponding author. Email: shiying@nepu.edu.cn

Abstract. Advances in computational capabilities as well as ongoing improvements in storage strategies have made reverse time migration (RTM) a feasible method for capturing images of complex structures. However, large storage requirements still restrict RTM applications, especially in anisotropic media. Utilising a first-order quasi-P-wave equation in vertically transversely isotropic (VTI) media, we investigate anisotropy and deduce an RTM equation for a staggered-grid high-order finite difference (FD) scheme incorporating a perfectly matched layer (PML) boundary in this study. We also develop an improved source wavefield storage strategy via a PML boundary method for VTI medium RTM using graphic processing unit (GPU) accelerated computation. Our proposed method significantly reduces the total volume of data storage required for conventional RTM while increasing calculation time by just a small amount. Checkpoints can be set based on GPU memory size, leading to the generation of high precision and high efficiency subsurface images. We carried out a series of numerical tests on simple anisotropic media and complex Hess 2D VTI models to verify the effectiveness of our proposed method.

Key words: GPU, PML, reverse time migration, storage, VTI.

Received 24 January 2017, accepted 23 January 2018, published online 16 April 2018

Introduction

The reverse time migration (RTM) method was first proposed in the 1980s (Baysal et al., 1983; McMechan, 1983; Whitmore, 1983) and now plays an important role in seismic imaging. Initially, RTM applications were restricted to post-stack datasets, but subsequent developments in computer hardware have led to the increasing use of these methods in research. However, due to subsurface material complexity, RTM assuming isotropy has achieved a relatively poor level of imaging accuracy. Enhancements can be achieved by focusing on RTM in anisotropic media.

In conventional RTM applications, wavefields are extrapolated using a numerical approach and an imaging condition is applied. Thus, one commonly applied technique is to construct source and receiver wavefields at each time point using the finite difference (FD). In a vertically transversely isotropic (VTI) medium, source and receiver wavefields are constructed by solving VTI equations (Duveneck et al., 2008; Liu and Sen, 2010; Pestana et al., 2012; Yan and Liu, 2013; Xie et al., 2014), and this medium is often used to represent an anisotropic model. Consistent with this practice, we focused on RTM of the first-order quasi-P-wave equation in VTI media. In this context, rather than developing a significantly computationally expensive anisotropic elastic equation, Alkhalifah (1998, 2000) started with an initial dispersion relationship and proposed a pseudo-acoustic approximation in a transversely isotropic medium by setting S-wave velocity at zero along the symmetry-axis. Subsequently, building on Alkhalifah's (1998, 2000) pseudo-acoustic approximation, second-order partial differential equations formulations have been developed to allow for VTI media (Zhou et al., 2006; Du et al., 2008). However, these formulations consider that the interfering SV-wave comprises an extra wavefield, and Hestholm (2007, 2009) proposed an acoustic VTI modelling method that utilises a straightforward numerical implementation of six first-order coupled partial differential equations; it is noteworthy, however, that FD, finite-element and pseudospectral approaches are all applicable to them.

Data storage requirements and computational cost are two main issues associated with RTM. The forward propagation wavefield and its backward propagation counterpart are normally calculated first, where a perfectly matched layer (PML) absorbing boundary around the domain of interest attenuates the wavefield within the damping region (Collino and Tsogka, 2001; Wang, 2003). Thus, if a cross-correlational RTM imaging condition is applied, the forward propagation wavefield for each time slice must be saved, necessitating a large amount of data storage. Attempts to reduce RTM storage include the work of Symes (2007), who outlined an optimal checkpoint scheme to reduce the need for data storage, although this scheme significantly increases the computational cost of RTM (Dussaud et al., 2008). Random boundaries (Clapp, 2009) can also be used to reduce wavefield storage but incur a double computational cost and introduce artefacts into final RTM images. Feng and Wang (2012) proposed the use of an approximately reconstructed source wavefield that utilises a single layer within the outer faces of the simulation area, sacrificing spatial accuracy near to boundaries. Sun and Fu (2013) employed a compression algorithm that was not subject to losses and also stored fewer time samples to reduce data storage. Although the two approaches proposed by Sun and Fu (2013) are feasible, balancing storage and computation is still necessary, especially in the case of 3D RTM. The recent rapid development of graphic

Journal compilation © ASEG 2018

processing units (GPUs) has greatly enhanced the computational efficiency of data processing (Han and Sun, 2015; Schiemenz and Igel, 2013; Shin et al., 2014) and also provides opportunities for RTM development. Indeed, a staggered-grid FD method for improving simulation accuracy was also previously described for simulating SH-wave (Virieux, 1984) and P-SV-wave (Virieux, 1986) propagation in heterogeneous media.

We present a first-order partial differential equation for the use of RTM in VTI media in this study and utilise staggered-grid FD to implement numerical computation and approximate temporal partial derivatives with second-order FD, as well as spatial partial derivatives with a high-order FD. We then discuss the use of an improved source wavefield storage strategy for RTM in a pseudo-anisotropic VTI media. Our approach is to perform forward wavefield propagation twice, saving six variables on a central processing unit (CPU) memory at each checkpoint during initial forward wavefield propagation. We then perform second forward wavefield propagation from the previous to subsequently checkpoint during the backward step, saving the stress wavefield P with just several grids near to boundary between two checkpoints on a GPU memory. We then apply GPU acceleration to improve computational efficiency and tested our proposed method using a series of simulation examples. Tests using a Hess 2D VTI model confirm the validity of our proposed RTM method.

Theory and methodology

The first-order partial differential equation for VTI media

The six first-order coupled 2D acoustic VTI wave equations are as follows (Hestholm, 2009):

$$\begin{aligned}
\frac{\partial v_x}{\partial t} &= -\frac{1}{\rho}\frac{\partial P}{\partial x}\\
\frac{\partial v_z}{\partial t} &= -\frac{1}{\rho}\frac{\partial P}{\partial z}\\
\kappa &= -\rho\frac{\partial v_x}{\partial x}\\
\frac{\partial \varphi}{\partial t} &= \frac{\partial \kappa}{\partial z}\\
\frac{\partial \zeta}{\partial t} &= \varphi\\
\frac{\partial P}{\partial t} &= (1+2\eta)v_{nmo}^2\kappa - v_v^2\rho\frac{\partial v_z}{\partial z} - 2\eta v_{nmo}^2 v_v^2\frac{\partial \zeta}{\partial z}.
\end{aligned} \tag{1}$$

In these expressions, P denotes stress, t is time, ρ is density, x and z refer to spatial directions, v_x and v_z are particle velocities in two directions, δ and ε are the Thomsen anisotropy parameters (Thomsen, 1986), κ, φ and ζ are medial variables, v_{nmo} is the normal moveout velocity, v_v and v_h are the vertical and horizontal velocities of the quasi-P-wave, and η is the anisotropy parameter. It therefore follows that:

$$\begin{aligned}
v_{nmo} &= v_v\sqrt{1+2\delta}\\
v_h &= v_v\sqrt{1+2\varepsilon}\\
\eta &= 0.5\left(\frac{v_h^2}{v_{nmo}^2}-1\right) = \frac{\varepsilon-\delta}{1+2\delta}.
\end{aligned} \tag{2}$$

On the basis of these expressions it is possible to derive a staggered-grid FD expression (Virieux, 1986), as outlined in Appendix A. We performed seismic modelling and RTM in VTI media using these equations.

Improved source wavefield storage strategy

Application of RTM usually requires time-forward source wavefield propagation (from time 0 to time $t_{\max}$), while receiver wavefield propagation occurs backward in time (from time $t_{\max}$ to time 0). Correlation of these two fields at each time point therefore presents a series of storage challenges; for example, 2D data for a 2000 by 1000 grid in x and y directions encompassing 10 000 time steps will require 80 GB of storage for the source wavefields that record propagation history. Thus, the storage requirement for RTM experiments based on 3D data presents an even greater challenge.

The strategy that we propose to reduce storage requirements using the PML absorbing boundary preserved a series of checkpoints wavefield within all the simulation domain obtained from initial forward propagation, and the boundary wavefield between adjacent checkpoints is obtained by using the checkpoints wavefield (the second forward modelling). The control equations for PML in acoustic VTI media are as follows:

$$\begin{aligned}
\frac{\partial v_x}{\partial t} + d(x)v_x &= -\frac{1}{\rho}\frac{\partial P_x}{\partial x}\\
\frac{\partial v_z}{\partial t} + d(z)v_z &= -\frac{1}{\rho}\frac{\partial P_z}{\partial z}\\
\kappa &= -\rho\frac{\partial v_x}{\partial x}\\
\frac{\partial \varphi_x}{\partial t} + d(x)\varphi_x &= 0\\
\frac{\partial \varphi_z}{\partial t} + d(z)\varphi_z &= \frac{\partial \kappa}{\partial z}\\
\frac{\partial \zeta_x}{\partial t} + d(x)\zeta_x &= \varphi_x\\
\frac{\partial \zeta_z}{\partial t} + d(z)\zeta_z &= \varphi_z\\
\frac{\partial P_x}{\partial t} + d(x)P_x &= (1+2\eta)v_{nmo}^2\kappa\\
\frac{\partial P_z}{\partial t} + d(z)P_z &= -v_v^2\rho\frac{\partial v_z}{\partial z} - 2\eta v_{nmo}^2 v_v^2\frac{\partial \zeta}{\partial z}\\
P &= P_x + P_z\\
\varphi &= \varphi_x + \varphi_z\\
\zeta &= \zeta_x + \zeta_z.
\end{aligned} \tag{3}$$

Thus, $d(x)$ and $d(z)$ are attenuation coefficients in the x and z directions in these expressions, while P_x and P_z are components of P, φ_x and φ_z are components of φ and ζ_x and ζ_z are components of ζ.

It is noteworthy that GPUs have better computational performance and bandwidth but smaller memory than CPUs; this may lead to extra costs if frequent data transfer is required between the two kinds of units when the wavefield data volume exceeds device memory. To ameliorate this issue, taking into account device memory size and wavefield recomputation ratio, we determined NC+1 checkpoints (where NC is the number of checkpoints for the numerical modeling time) at time points where the entire checkpoints wavefield including six variables is saved to the host memory during the forward propagation of source wavefields, as shown in Figure 1. In this case, the boundary stress wavefield P was saved on a device memory at every time step between two adjacent checkpoints during the second stage of wavefield forward propagation.

Figure 2 shows the scheme for improving source wavefield storage. In this approach, the PML boundary is located in the grey domain between the dotted line and the outer solid line, as shown in Figure 2*a*, while the green domain wavefield falls between the two solid lines located in the boundary grids of the undamped computational domain and saved at each time step on the device memory. In contrast with previous methods (e.g. Feng and Wang, 2012), however, this method saves the boundary wavefield from the computational rather than the PML-absorbing domain, which means that no energy is attenuated from the saved boundary wavefield and relatively little storage space is required.

We perform the RTM of the first-order quasi-P-wave equation in VTI media. Thus, the wave-equation group comprises just first-order partial differential equations, which enables high-order FD calculations to be performed on discrete grids. Six variables needed to be updated at each time step including the stress wavefield P, the velocities v_x and v_z and the medial variables κ, φ and ζ, all of which require extensive data storage. Therefore, if a boundary-saving scheme can be used that only saves

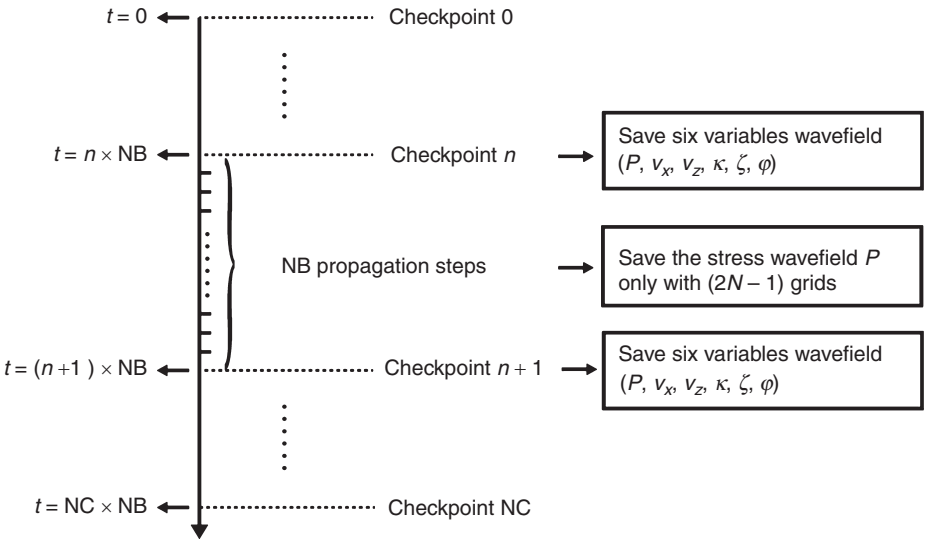

Fig. 1. Schematic to illustrate the checkpoint set and six variables wavefield storage used in this study. Taking into account device memory size and recomputation ratio, NC+1 checkpoints can be determined at time points where the entire checkpoints wavefields including the six variables is saved to the host memory during the forward propagation of source wavefields. For the NB propagation steps between two adjacent checkpoints, save the stress wavefield P only with $(2N - 1)$ grids.

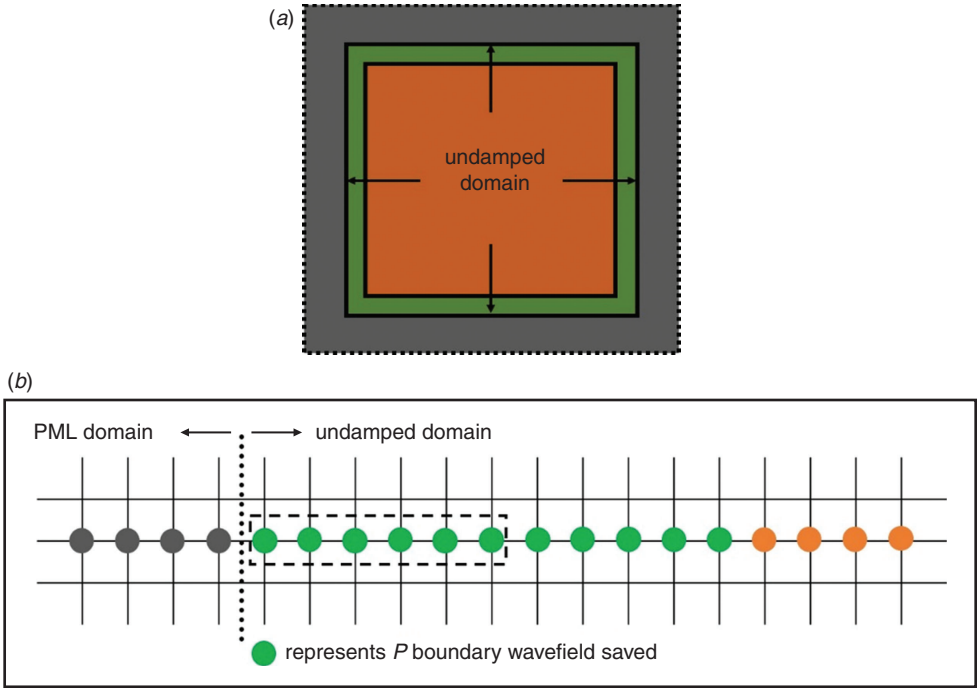

Fig. 2. Improved source wavefield storage strategy by PML boundary: (*a*) The PML boundary is located in the grey domain between the dotted line and the outer solid line, while the green domain wavefield falls between the two solid lines located in the boundary grids of the undamped computational domain and saved at each time step on device memory. (*b*) The stress wavefield P with $(2N - 1)$ grids is saved along the green margin of the undamped domain.

snapshots of the six variables at checkpoints on a host memory as well as the stress boundary wavefield P between two checkpoints on a device memory, extensive storage redundancies can be eliminated.

The green domain in Figure 2*b* denotes cells for which the boundary source wavefield between two checkpoints is saved during the second stage of forward propagation. In this case, the six boundary field variables, P, v_x, v_z, κ, φ and ζ must be saved even though these normally complicate the algorithm and require increased data storage. Depending on the FD order, it is possible to determine the width of the green domain; thus, a higher order of approximation in the space domain is represented by increased width of the green domain.

However, because these variables are interdependent, ensuring the accuracy and integrity of the P boundary wavefield inside the simulation domain during the second stage of forward propagation also means that the other five variables will be accurate. We employed an approximation of order $2N$ in the space domain to save the stress boundary wavefield variable P with $(2N - 1)$ grids along the margin of the undamped domain. Incorporation of this step allowed us to calculate the other five variables with N grids along the boundary, illustrated as green points inside a dashed frame (Figure 2*b*). Thus, during backward wave propagation, we re-inject the saved stress wavefield with $(2N - 1)$ grids, which ensures that the other five are correct during variable updates.

Figure 3 presents the basis for saving the stress wavefield P with $(2N - 1)$ grids using Equation A-1. We calculated v_x using P during backward wavefield propagation so that v_x is accurate inside the red dashed frame. Similarly, we can calculate v_z using P during backward wavefield propagation so that v_z is accurate inside the blue dashed frame. Depending on the accuracy of v_x within the red dashed frame, we then calculated κ, which ensures that κ is accurate within the green dashed frame. It is then possible to calculate φ and ζ, because κ is accurate within the green dashed frame, which ensures that φ and ζ are accurate within the purple dashed frame. Thus, based on this analysis, the variables v_x, v_z, κ, φ and ζ are all correct within the purple dashed frame. We then calculated the correct stress wavefield P for the next time step within a shallow region using the variables v_x, v_z, κ, φ and ζ within the purple dashed frame. At each different time step, P is then correct within the shallow region, and so we saved $(2N - 1)$ boundary grids for the stress wavefield P on a device memory during the second forward wavefield propagation. Finally, we re-inject the saved boundary stress wavefield P with $(2N - 1)$ grids during backward wavefield propagation. We can control the memory of boundary stress wavefield P with $(2N - 1)$ grids with NB time steps (NB is the number of propagation steps between two adjacent checkpoints), as shown in Figure 1, and we store the boundary stress wavefield P on device memory rather than store in host memory to avoid frequent data exchange.

A corresponding simulation for an acoustic anisotropic VTI medium is shown in Figure 4. In this example, we placed a source at the centre of the 2D model that incorporates a 200 by 200 grid in the x and z directions and has uniform 10 m grid intervals for dx and dz. The dominant frequency of the Ricker wavelet is 20 Hz. This model is surrounded by PML boundaries so that 50 grid-points wide absorbing layers are set around the simulation domain. Forward propagation source and the re-generated source wavefields at $t = 0.18$ s, $t = 0.27$ s, $t = 0.43$ s and $t = 0.6$ s are compared in Figure 4. Figure 4*a* shows

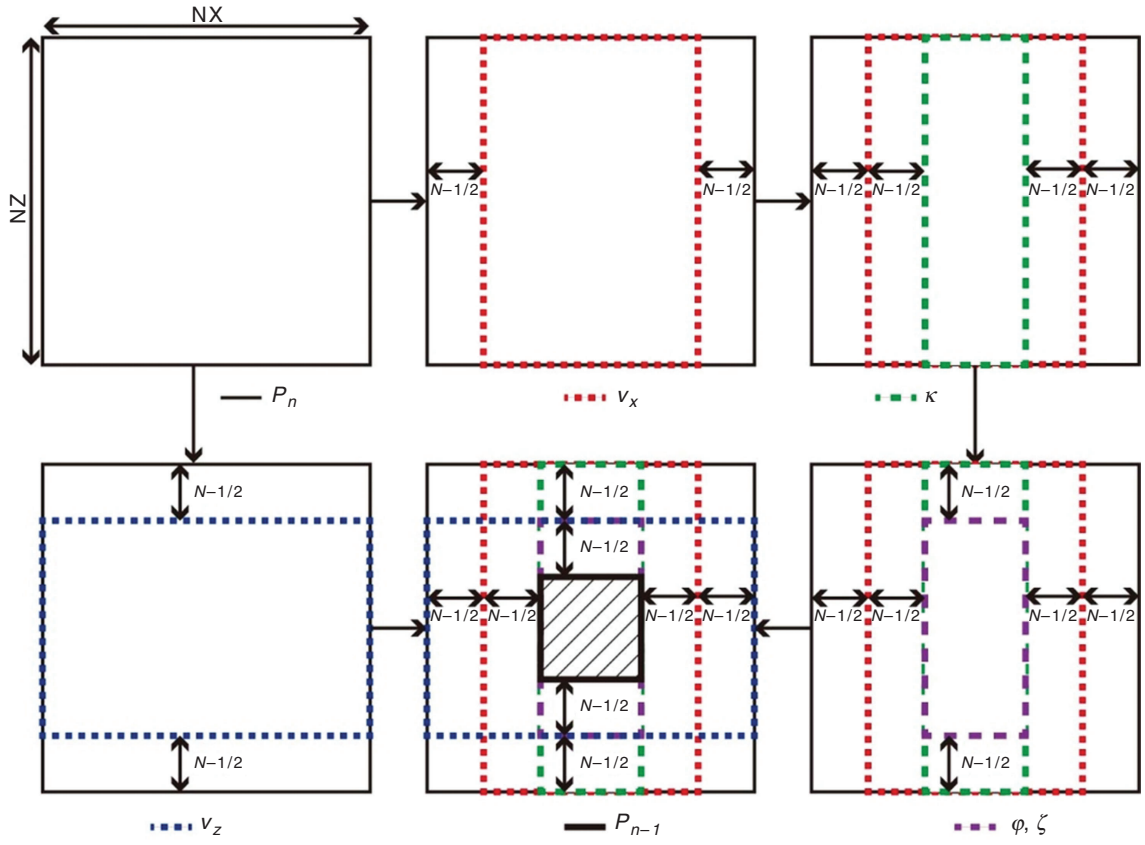

Fig. 3. Schematic to illustrate saving the stress wavefield P with $(2N - 1)$ grids. Based on the stress wavefield P along the margin of the undamped domain, the other five variables along the boundary can be calculated.

the forward-propagated source wavefield, while Figure 4*b* illustrates the backward-propagated source wavefield using the improved PML absorbing boundary. This approach yielded perfect results in the undamped simulation zone.

Results show that when the wavefield is extracted along the red line in Figure 4 (as shown in Figure 5), the forward-propagation source (red solid line) and the backward-propagation source wavefield (black dashed line) are in close agreement. This demonstrates the applicability of our proposed method for RTM imaging in VTI and its ability to save a great deal of data storage space.

Simulated examples

In order to verify the capabilities of 2D acoustic VTI RTM, we tested a 2D Hess model (Figure 6) that contains vertical P-wave velocity as well as the anisotropy parameters ε and δ. In this case, we set the grid size to 3617 by 1500 with a uniform spatial interval of 20 ft in the x and z directions using a Ricker wavelet source with a dominant frequency of 30 Hz and a shot interval of 100 ft. We then used staggered-grid FD methods that had second-order temporal accuracy and twelfth-order spatial accuracy for numerical modelling, RTM for the 2D Hess VTI model with a time step of 0.3 ms and a PML boundary width of 50 grids. The GPU accelerator environment used in this simulation was a Nvidia Tesla K10 with each card comprising two GPU kernels, each with 4 GB graphic memory and a single-precision performance of 2288 GFLOPS. At the same time, we used nine GPU kernels for modelling and RTM; to compare computational efficiencies, we carried out wavefield modelling of the Hess 2D VTI model on a XEON E5–2630 CPU that had a 2.3 GHz clock speed and a combined GPU/CPU. In the case of 1000 propagation steps of shot modelling, the CPU took 26 242 s, while GPU/CPU collaborative parallel computing took 261 s, a speedup ratio of ~100 times.

We implemented anisotropic RTM using six coupled first-order partial differential equations for acoustic VTI media; the RTM profile comprising 723 shots after Laplace filtering is shown in Figure 7. The test presented in this paper demonstrates that our proposed VTI RTM method is both applicable and robust.

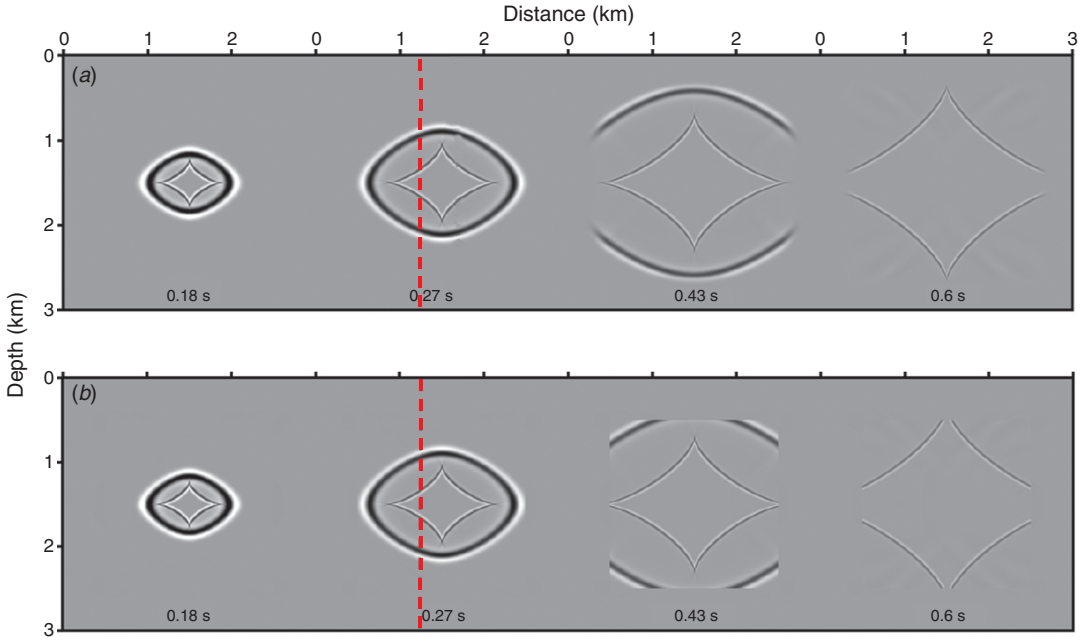

Fig. 4. Snapshot of homogeneous anisotropic medium model at 0.18 s, 0.27 s, 0.43 s and 0.6 s: (*a*) forward-propagated source wavefield; (*b*) backward-propagated source wavefield using the improved PML absorbing boundary.

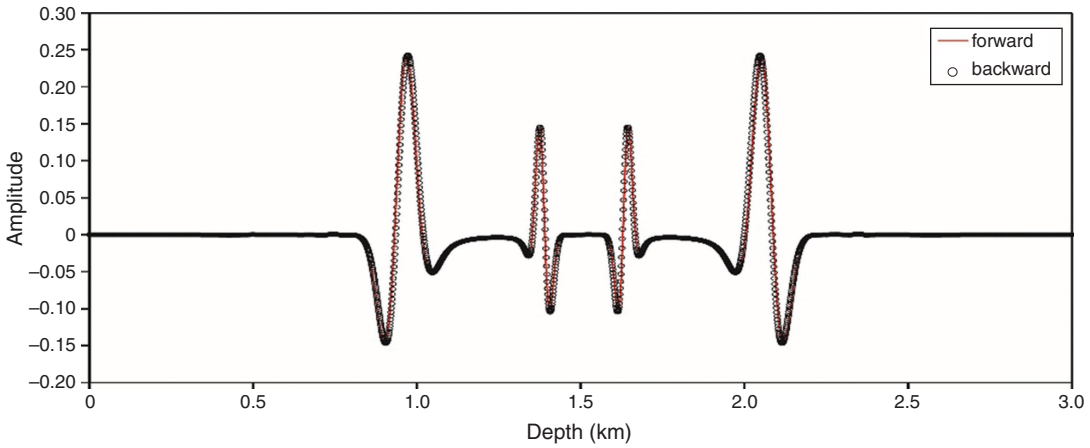

Fig. 5. Wavefield along the red dashed line in Figure 4.

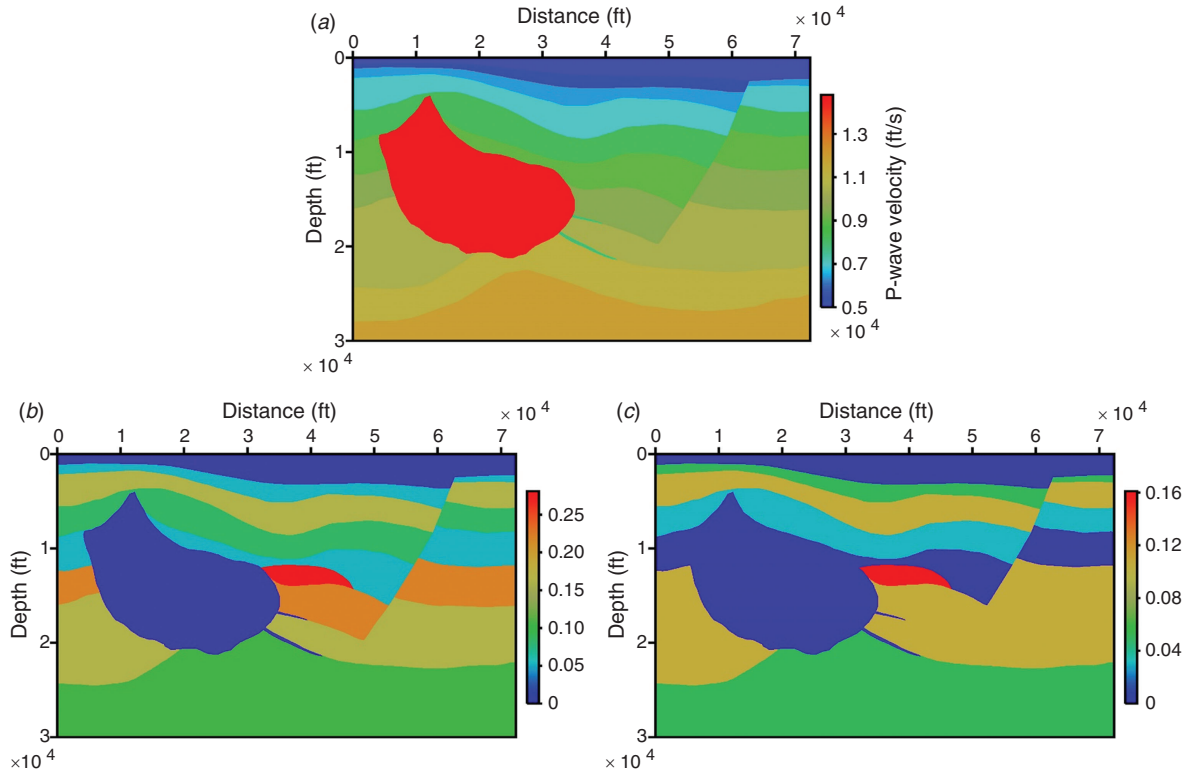

Fig. 6. Anisotropic Hess model: (*a*) velocity model; (*b*) anisotropy parameter ε; (*c*) anisotropy parameter δ.

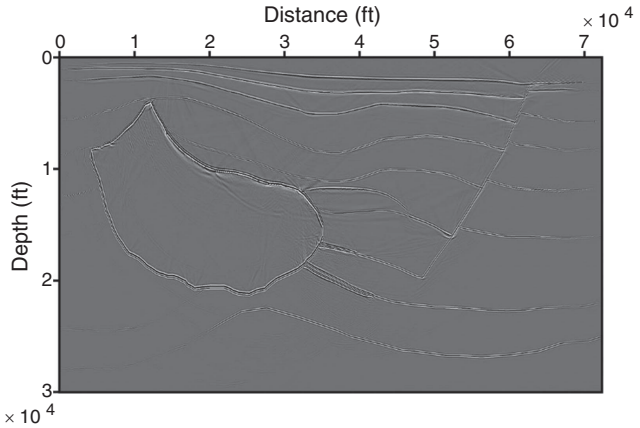

Fig. 7. RTM profiles for the 2D Hess VTI model.

Conclusions

As the subsurface is largely anisotropic, it is necessary to consider the effects of anisotropic media when using RTM. Thus, we present an acoustic VTI RTM approach in this study that exhibits an improved wavefield storage strategy using first-order coupled acoustic VTI wave equations. Our strategy saves the checkpoint wavefields in a host memory and the boundary wavefields on a device memory that greatly incorporates PMLs and thus decreases storage costs. We are therefore able to control checkpoints based on GPU memory size to enable optimised computation efficiency while at the same time utilise a staggered-grid FD within RTM. The method proposed in this paper generates high-precision imaging and has suitable data storage capacity for use in a VTI media.

Conflicts of interest

The authors declare no conflicts of interest.

Acknowledgements

This research was supported by a Project of the National Natural Science Foundation of China (grant nos 41574117, 41474118), the Excellent Youth Foundation of Heilongjiang Province, China (grant no. JC2016006) and The Northeast Petroleum University Excellent Scientific Talent Fund (grant no. GLJHB201601).

References

Alkhalifah, T., 1998, Acoustic approximations for processing in transversely isotropic media: *Geophysics*, **63**, 623–631. doi:10.1190/1.1444361

Alkhalifah, T., 2000, An acoustic wave equation for anisotropic media: *Geophysics*, **65**, 1239–1250. doi:10.1190/1.1444815

Baysal, E., Kosloff, D., and Sherwood, J., 1983, Reverse time migration: *Geophysics*, **48**, 1514–1524. doi:10.1190/1.1441434

Clapp, R. G., 2009, Reverse time migration with random boundaries: SEG Technical Program Expanded Abstracts, 2809–2813.

Collino, F., and Tsogka, C., 2001, Application of the perfectly matched absorbing layer model to the linear elastodynamic problem in anisotropic heterogeneous media: *Geophysics*, **66**, 294–307.

Du, X., Fletcher, R. P., and Fowler, P. J., 2008, A new pseudo-acoustic wave equation for VTI media: 70th EAGE Conference and Exhibition, Extended Abstracts, H033.

Dussaud, E., Symes, W. W., Williamson, P., Lemaistre, L., Singer, P., Denel, B., and Cherrett, A., 2008, Computational strategies for reverse-time migration: SEG Technical Program Expanded Abstracts, 2267–2271.

Duveneck, E., Milcik, P., Bakker, P. M., and Perkins, C., 2008, Acoustic VTI wave equations and their application for anisotropic reverse-time migration: SEG Technical Program Expanded Abstracts, 2186–2190.

Feng, B., and Wang, H., 2012, Reverse time migration with source wavefield reconstruction strategy: *Journal of Geophysics and Engineering*, **9**, 69–74. doi:10.1088/1742-2132/9/1/008

Han, F., and Sun, S. Z., 2015, GPU acceleration of amplitude-preserved Q compensation prestack time migration: *Computers & Geosciences*, **82**, 214–224. doi:10.1016/j.cageo.2015.06.018

Hestholm, S., 2007, Acoustic VTI modeling using high-order finite-differences: SEG Technical Program Expanded Abstracts, 139–143.

Hestholm, S., 2009, Acoustic VTI modeling using high-order finite-differences: *Geophysics*, **74**, T67–T73. doi:10.1190/1.3157242

Liu, Y., and Sen, M. K., 2010, Acoustic VTI modeling with a time-space domain dispersion-relation-based finite-difference scheme: *Geophysics*, **75**, A11–A17. doi:10.1190/1.3374477

McMechan, G., 1983, Migration by extrapolation of time-dependent boundary values: *Geophysical Prospecting*, **31**, 413–420. doi:10.1111/j.1365-2478.1983.tb01060.x

Pestana, R. C., Ursin, B., and Stoffa, P. L., 2012, Rapid expansion and pseudo spectral implementation for reverse time migration in VTI media: *Journal of Geophysics and Engineering*, **9**, 291–301. doi:10.1088/1742-2132/9/3/291

Schiemenz, A., and Igel, H., 2013, Accelerated 3-D full-waveform inversion using simultaneously encoded sources in the time domain: application of Valhall ocean-bottom cable data: *Geophysical Journal International*, **195**, 1970–1988. doi:10.1093/gji/ggt362

Shin, J., Ha, W., Jun, H., Min, D. J., and Shin, C., 2014, 3D Laplace-domain full waveform inversion using a single GPU card: *Computers & Geosciences*, **67**, 1–13. doi:10.1016/j.cageo.2014.02.006

Sun, W., and Fu, L., 2013, Two effective approaches to reduce data storage in reverse time migration: *Computers & Geosciences*, **56**, 69–75. doi:10.1016/j.cageo.2013.03.013

Symes, W. W., 2007, Reverse time migration with optimal checkpointing: *Geophysics*, **72**, SM213–SM221. doi:10.1190/1.2742686

Thomsen, L., 1986, Weak elastic anisotropy: *Geophysics*, **51**, 1954–1966. doi:10.1190/1.1442051

Virieux, J., 1984, SH-wave propagation in heterogeneous media: Velocity-stress finite-difference method: *Geophysics*, **49**, 1933–1942. doi:10.1190/1.1441605

Virieux, J., 1986, P-SV wave propagation in heterogeneous media: Velocity-stress finite-difference method: *Geophysics*, **51**, 889–901. doi:10.1190/1.1442147

Wang, S. D., 2003, Absorbing boundary condition for acoustic wave equation by perfectly matched layer: *Oil Geophysical Prospecting*, **38**, 31–34. [in Chinese]

Whitmore, D., 1983, Iterative depth migration by backward time propagation: SEG Technical Program Expanded Abstracts, 382–385.

Xie, W., Yang, D., Liu, F., and Li, J., 2014, Reverse-time migration in acoustic VTI media using a high-order stereo operator: *Geophysics*, **79**, WA3–WA11. doi:10.1190/geo2013-0224.1

Yan, H., and Liu, Y., 2013, Acoustic VTI modeling and pre-stack reverse-time migration based on time-space domain staggered-grid finite-difference method: *Journal of Applied Geophysics*, **90**, 41–52. doi:10.1016/j.jappgeo.2012.12.008

Zhou, H., Zhang, G., and Bloor, R., 2006, An anisotropic acoustic wave equation for VTI media: 68th EAGE Conference and Exhibition incorporating EUROPEC, Extended Abstracts, 1171–1174.

Appendix A

Staggered-grid difference expression

In this study, v_x, v_z and κ are defined at the time levels $n+1/2$ and $n-1/2$, while φ is defined for time levels n, $n-1$, ζ is defined for time levels $n-1/2$, $n-3/2$, and P is defined for time levels n, $n+1$.

The staggered-grid expressions used in this study that are second-order in time and $2N$ order in space (Virieux, 1986) are as follows:

$$
\begin{aligned}
v^{n+1/2}_{x(i+1/2,j)} &= v^{n-1/2}_{x(i+1/2,j)} - \frac{\Delta t}{\Delta x \rho_{(i+1/2,j)}} \sum_{m=1}^{N} C_m^N \left[P^n_{(i+m,j)} - P^n_{(i-m+1,j)} \right] \\
v^{n+1/2}_{z(i,j+1/2)} &= v^{n-1/2}_{z(i,j+1/2)} - \frac{\Delta t}{\Delta z \rho_{(i,j+1/2)}} \sum_{m=1}^{N} C_m^N \left[P^n_{(i,j+m)} - P^n_{(i,j-m+1)} \right] \\
\kappa^{n+1/2}_{i,j} &= -\frac{\rho_{(i,j)}}{\Delta x} \sum_{m=1}^{N} C_m^N \left[v^{n+1/2}_{x(i+m-1/2,j)} - v^{n+1/2}_{x(i-m+1/2,j)} \right] \\
\varphi^{n}_{i,j+1/2} &= \varphi^{n-1}_{i,j+1/2} + \frac{\Delta t}{\Delta z} \sum_{m=1}^{N} C_m^N \left[\kappa^{n-1/2}_{x(i,j+m)} - \kappa^{n-1/2}_{x(i,j-m+1)} \right] \\
\zeta^{n-1/2}_{i,j+1/2} &= \zeta^{n-3/2}_{i,j+1/2} + \Delta t \varphi^{n-1}_{i,j+1/2} \\
P^{n+1}_{(i,j)} &= P^n_{(i,j)} + \Delta t (1 + 2\eta_{(i,j)}) v^2_{nmo(i,j)} \kappa^{n+1/2}_{(i,j)} \\
&\quad - v^2_{v(i,j)} \rho_{(i,j)} \frac{\Delta t}{\Delta z} \sum_{m=1}^{N} C_m^N \left[v^{n+1/2}_{z(i,j+m-1/2)} - v^{n+1/2}_{z(i,j-m+1/2)} \right] \\
&\quad - 2\eta_{(i,j)} v^2_{nmo(i,j)} v^2_{v(i,j)} \frac{\Delta t}{\Delta z} \sum_{m=1}^{N} C_m^N \left[\zeta^{n+1/2}_{(i,j+m-1/2)} - \zeta^{n+1/2}_{(i,j-m+1/2)} \right].
\end{aligned}
\tag{A-1}
$$

In these expressions, Δx and Δz are the discrete spatial step sizes in the x and z directions, respectively, while Δt is the discrete time step size, n is the propagation step and C_m^N is the staggered-grid difference coefficient.